Modeling electrochemical partial oxidation of methane for cogeneration of electricity and syngas in solid-oxide fuel cells

Huayang Zhu[a,*], Robert J. Kee[a], Manoj R. Pillai[b,c], Scott A. Barnett[b]

[a] Colorado School of Mines, 1500 Illinois Street, Golden, CO 80401, USA
[b] Northwestern University, Evanston, IL 60208, USA
[c] Functional Coating Technology, Evanston, IL 60201, USA

ABSTRACT

This paper uses computational models to evaluate strategies for scaling electrochemical partial oxidation (EPOX) processes from the laboratory scale to practical application. In addition to producing electrical energy alone, solid-oxide fuel cells (SOFC) can be operated with hydrocarbon fuel streams to produce synthesis gas (H_2 and CO) as well. SOFC systems are usually operated to consume most of the fuel and produce electricity. However, by operating with a hydrocarbon fuel at relatively high flow rates, the exhaust-gas composition can be predominantly syngas. In this case the steam (and CO_2), produced from electrochemical and thermal reactions, reacts to reform the hydrocarbon fuel within the catalytic anode support structure. A practical limitation of electrochemical partial oxidation operation is the fact that carbon tends to deposit on Ni-based anode catalysts. The present paper explores the use of barrier layers to prevent carbon deposits. The results show that a tubular cell can be designed to deliver syngas and electricity using methane as the primary fuel.

© 2008 Elsevier B.V. All rights reserved.

1. Introduction

Solid-oxide fuel cells (SOFC) are usually designed and operated to consume fuel and produce only electricity. However, they can be used for alternative purposes. For example, SOFC systems can be operated as chemical reactors to produce a variety of useful chemicals depending on fuel mixtures and operating conditions [1–4]. There has been interest in SOFC operation as an electrochemical partial oxidation (EPOX) reactor where both electric power and syngas are desired products. Similar to catalytic membrane reactors [5–9], this approach has advantages compared to conventional CH_4 partial oxidation to syngas using air. Because CH_4 and O_2 are not premixed, the potential for hazardous explosion is eliminated, and the SOFC reacts the fuel with pure O_2, eliminating any need for N_2 separation from the syngas. The fact that the SOFC yields two products increases its economic value; that is, the device could be sold at a substantially higher price than a similar electricity-only SOFC [9]. Another potentially useful feature is that selectivity between electricity and syngas could be controlled to meet varying demands. EPOX has been demonstrated at the button-cell level [1,4,9–12], and in one case [7], a stack was shown to produce syngas from methane.

In addition to co-production of electricity and syngas, there is also interest in similar technologies for the co-production of electricity and hydrogen [13–16].

The primary objective of this paper is to investigate important issues related to scaling a methane-fed EPOX system from laboratory-scale button cells to more practical devices and systems. The paper uses computational models to explore design and operating alternatives. The approach begins by developing and validating models for the button-cell experiments. These models are then used to predict performance for larger devices and alternative geometries. Indeed a particular strength of physical models is that validated results in one geometry can be confidently mapped to other geometries. This paper concentrates on anode-supported tubes, which is an attractive configuration for EPOX since the exhaust gases must be collected. Barrier layers, which assist in the prevention of carbon deposits on Ni–YSZ anodes, are an important element of the design and scaling approach.

In broad terms, the partial oxidation of methane to form syngas in a SOFC is a two-step process. Steam is first formed as the product of H_2 electro-oxidation. This steam is then available to reform methane within a Ni–YSZ porous, composite, anode structure. Although on-anode hydrocarbon reforming is the subject of much research, to our knowledge an EPOX model has not been reported. The models used in the present effort provide great detail in thermal chemistry, electrochemistry, porous-media transport,

* Corresponding author. Tel.: +1 303 273 3890; fax: +1 303 273 3602.
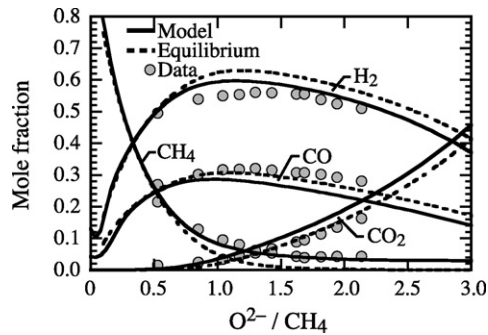*E-mail address:* hzhu@mines.edu (H. Zhu).

Fig. 1. Measured exhaust composition in a button-cell experiment as a function of the molar-flux ratio of O^{2-} through MEA structure and the inlet CH_4 flow. The dashed lines show the equilibrium composition and the solid lines are model predictions. The cell is operating at $750°C$ and 1 atm.

and fluid flow. Such models can play important roles in the extension of EPOX from the current button-cell level to the stack level.

Several critical issues, where EPOX operation is fundamentally different from conventional SOFC operation, can be investigated via modeling. First, given the range of reactions and products possible, it is important to extrapolate from button-cell results to stack-level systems, evaluating design and operating conditions that yield the desired syngas composition. Second, because EPOX requires introduction of nearly dry methane into the SOFC, it is important to find stack configurations and operating conditions to avoid anode coking. While button-cell tests have shown stable non-coking EPOX operation, the extension to a stack can be difficult. Third, because H_2 is likely produced by CH_4 reforming with electrochemical reaction products, it is important to determine if the H_2 concentration near the fuel inlet is sufficient to produce reasonably uniform current density throughout the stack. Fourth, because the EPOX process includes both exothermic electrochemical processes and endothermic reforming chemistry, stack temperature profiles can be substantially different from those in a conventional SOFC. It is important to find conditions where temperature gradients are minimized, and where the stack is thermally self-sustaining. Self-sustained operation is potentially difficult because the partial oxidation chemistry is only mildly exothermic.

2. Partial oxidation and EPOX

EPOX selectivity to syngas depends upon the ratio of CH_4 flow rate and O^{2-} transport rate through the membrane–electrode assembly (MEA) structure. When electricity is the only desired output, the global reaction shows that the cell should be operated such that

$$CH_4 + 4O^{2-} \rightleftharpoons CO_2 + 2H_2O + 8e^-. \tag{1}$$
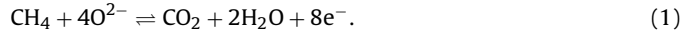
When syngas is the desired product, the global reaction indicates that the operating stoichiometry should be adjusted such that

$$CH_4 + O^{2-} \rightleftharpoons CO + 2H_2 + 2e^-. \tag{2}$$

The complete electrochemical oxidation of CH_4 (Eq. (1)) requires that the molar-flux ratio of O^{2-} to CH_4 is four, while partial oxidation to syngas requires a molar-flux ratio of unity. The cell operating conditions can be controlled to vary the molar-flux ratio, and hence the output fractions of syngas and electricity. Typically, the methane flux is varied while cell maintains the oxygen flux via the cell potential.

Using button-cell experiments, Pillai et al. [9,12] have reported EPOX performance as a function of the O^{2-}/CH_4 molar-flux ratio. Fig. 1 shows measured species mole fractions [12] together with the equilibrium mole fractions as functions of molar-flux ratio. These data are reported on a dry basis (i.e., H_2O removed) because the experiments remove H_2O prior to measurement. The figure also shows model predictions, which are discussed later in the paper.

Fig. 1 shows a maximum H_2 concentration at a molar-flux ratio of $O^{2-}/CH_4 \approx 1.2$. At lower molar-flux ratios, excess CH_4 remains in the exhaust. At higher molar-flux ratios, increasing levels of CO_2 and H_2O are delivered in the exhaust. In a full SOFC or EPOX stack (i.e., not a button cell), the current density (and hence O^{2-} flux) varies spatially, as a function of fuel depletion. Thus, a practical system must be designed to accommodate such variations within a cell.

3. EPOX design considerations

Because fuels with high hydrocarbon fractions are needed to promote selectivity to syngas, carbon deposits are a practical
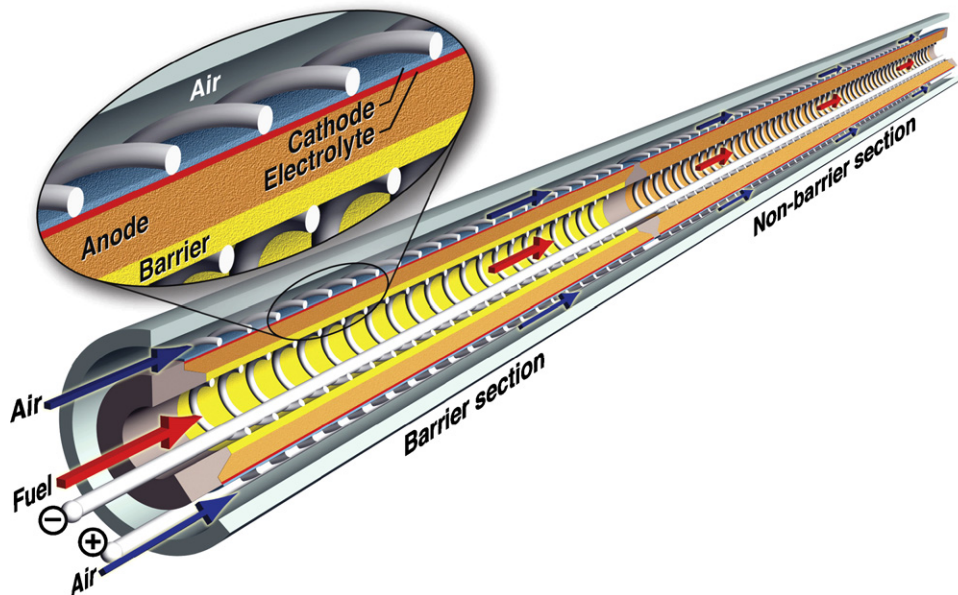

Fig. 2. Illustration of an anode-supported tubular solid-oxide fuel cell with a porous barrier layer in entrance region.

design concern for an EPOX system, particularly when low-cost Ni-based anodes are used. Barnett and colleagues have demonstrated that design innovations, such as anode barrier layers [17,18], and operating conditions, such as low cell voltage to increase steam production, lead to stable EPOX operation without deleterious deposit formation [9].

Another consideration for the EPOX design and operation concerns thermal balances and temperature variations. The catalytic reforming chemistry within the anode is endothermic. However, heat is also produced as a result of electrochemical charge-transfer reactions and ohmic heat generation associated primarily with ion transport. These thermal sources and sinks contribute to temperature variations in the system [19]. The temperature variations, in turn, affect the SOFC structure and performance, including product selectivity and long-term stability.

Fig. 2 illustrates an anode-supported tubular geometry. The porous-anode tube wall is fabricated as a Ni–YSZ cermet, with a thin dense YSZ electrolyte and porous LSM–YSZ cathode applied to the outside of the tube. A chemically inert barrier layer, made of an oxide-ceramic material, is used in the upstream portions of the tube. As illustrated in Fig. 2, air flow is confined within an annular region outside the cathode layer. However, there are certainly alternatives to such a design. For example, as is typical in tube-stack SOFC systems, many SOFC tubes can be arranged within a common chamber through which cathode air is circulated.

The role of the barrier is to trap electrochemically generated steam, such that the steam–carbon ratio is below the coking limit in the presence of Ni [17,18]. The barrier thus enables the use of undiluted hydrocarbons (here methane) in the fuel feeds. The barrier's physical characteristics (i.e., combination of porosity, primary particle diameter, pore radius, tortuosity, and thickness) are set to assure that when a hydrocarbon first comes into contact with Ni, the equilibrium formation of solid carbon is unfavorable.

As illustrated in Fig. 2 the barrier layer is electrically connected to the Ni–YSZ anode structure. Thus, with anode current collection on the inside of the tube, the barrier layer must have sufficient electronic conductivity. Certain pervoskite materials, such as doped strontium titanite, are good candidate materials [20]. However, if the barrier layer is not electronically conductive, then an alternative current collection approach is needed. For example, current collection could attached directly to the Ni–YSZ layer, with a loosely fitted barrier tube interior to the current collection. In any case, the objective of the present paper is to explore general possibilities for scaling EPOX systems beyond button-cell experiments, not to propose specific system designs.

4. Button cell experiments

Zhan et al. [9] and Pillai et al. [12] report button-cell experiments, demonstrating and characterizing the electrochemical partial oxidation of CH_4 to syngas in SOFCs (air, LSM–YSZ | YSZ |Ni–YSZ, CH_4). Fig. 3 is a schematic that shows the major features of the button-cell experiments. Fuel, supplied via a central tube, flows radially across the anode face of the MEA. Air is supplied to the cathode side of the MEA. The entire assembly is housed within a furnace, which maintains a fixed temperature.

The anode structure is composed of a 700 μm Ni–YSZ support layer and a 25 μm Ni–YSZ functional layer. The dense electrolyte is 10 μm of YSZ and the LSM–YSZ cathode is 40 μm thick. Fig. 4 shows measured polarization characteristics with the button cell operating on humidified H_2 at atmospheric pressure and temperatures of 700 °C, 750 °C, and 800 °C.

The button-cell experiments are used to establish representative parameters for the MEA structure that are used in the
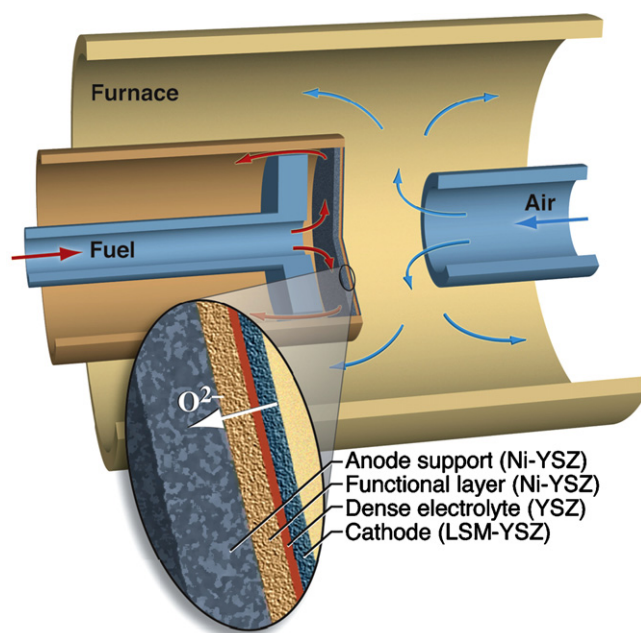

Fig. 3. Schematic representation of the EPOX button-cell experiment.

tubular model [19,21]. Many of the parameters are physical dimensions that are easily established. However, as with most models, other parameters are empirical. For example, parameters in the charge-transfer exchange current densities are not measured independently. Rather, they are adjusted to provide a good representation of measured polarization characteristics over a range of operating conditions. Parameters such as the porous-media tortuosity can be adjusted to assist representing concentration polarization at high current density. As seen in Fig. 4, the model represents the button-cell polarization characteristics well. Table 1 lists all the physical parameters that are used to characterize the MEA. In all cases the parameters are within reasonable ranges, and once fixed to represent the button-cell data are not changed again. Detailed definitions of the physical parameters in the MEA model are discussed by Zhu et al. [19,21].
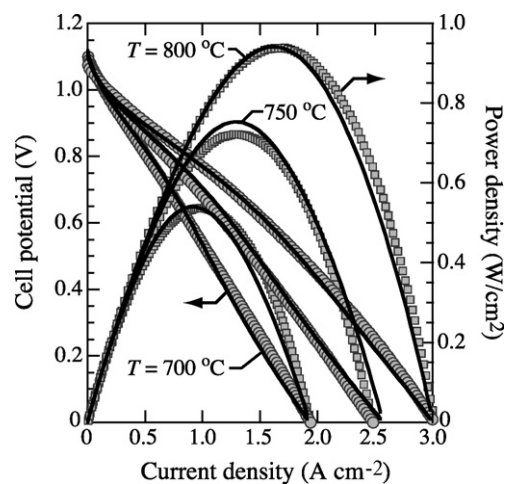

Fig. 4. Measured cell potential and power density as functions of current density for a button-cell MEA structure operating with a fuel of 97% H_2 and 3% H_2O at 1 atm and temperatures of 700 °C, 750 °C, and 800 °C. The oxidizer is air. The solid lines are the model predictions.

Table 1
Parameters for modeling the MEA structure

Parameters	Value	Units
Anode		
Thickness (L_a)	725	μm
Porosity (ϕ)	0.40	
Tortuosity (τ)	4.80	
Pore radius (r_p)	0.125	μm
Particle diameter (d_p)	1.00	μm
Specific catalyst area (A_s)	1.0E4	cm^{-1}
Exchange current factor ($i^*_{H_2}$)	2.25	A cm^{-2}
Activation energy (E_{H_2})	6.5E3	J mol^{-1}
Reference temperature (T_{ref})	750	°C
Anodic symmetry factor (α_a)	1.5	
Cathodic symmetry factor (α_c)	0.5	
Cathode		
Thickness (L_c)	40	μm
Porosity (ϕ)	0.30	
Tortuosity (τ)	5.40	
Pore radius (r_p)	0.125	μm
Particle diameter (d_p)	0.75	μm
Exchange current factor ($i^*_{O_2}$)	1.58	A cm^{-2}
Activation energy (E_{O_2})	7.9E3	J mol^{-1}
Reference temperature (T_{ref})	750	°C
Anodic symmetry factor (α_a)	0.86	
Cathodic symmetry factor (α_c)	0.14	
Electrolyte: $\sigma_{el} = \sigma_0 T^{-1} \exp(-E_{el}/RT)$		
Thickness (L_{el})	10	μm
Activation energy (E_{el})	8.0E4	J mol^{-1}
Ion conductive pre-factor (σ_0)	1.8E5	S cm^{-1}
Barrier		
Thickness (L_{el})	400	μm
Porosity (ϕ)	0.175	
Tortuosity (τ)	6.00	
Pore radius (r_p)	0.15	μm
Particle diameter (d_p)	0.80	μm

In addition to polarization characteristics (Fig. 4), the button-cell experiments also measure exhaust-gas composition [12]. Fig. 1 shows results from an experiment using a CH_4 fuel stream at atmospheric pressure and 750 °C. This figure also compares the data with predictions from the button-cell model and local equilibrium. The oxygen-ion flux is simply related to the measured current density i as $J_{O^{2-}} = i/2F$. The equilibrium compositions are computed at 750 °C and atmospheric pressure, constraining the atomic balance to be that associated with the measured CH_4 flux and current density. The button-cell model incorporates finite rate chemistry, electrochemistry, and porous-media transport.

It is evident from Fig. 1 that both the equilibrium and kinetics models provide reasonable predictions of the measured exhaust composition. In fact, both are likely within experimental error. The predictions of H_2 and CH_4 by the full model are closer to the measurements, indicating some kinetic or transport limitations in the process. However, the full model shows a larger discrepancy in the CO/CO_2 ratio.

5. Physical and chemical models

Because the mathematical model is documented in previous literature [19,21], only a brief summary is presented here. Gas flow within the tube is modeled as a one-dimensional plug flow, neglecting radial spatial variations and axial diffusion [22]. Homogeneous gas-phase chemistry is neglected owing to very low reaction rates for CH_4 at temperatures below around 900 °C [23]. The reacting porous-media transport is represented using a Dusty-gas model (DGM), which considers pressure-driven convective fluid flow as well as ordinary and Knudsen molecular diffusion [24]. Because axial porous-media transport is negligible compared to axial trans-

port by fluid flow in the tube, only radial porous-media transport is considered.

The heterogeneous chemistry of CH_4 reforming within the Ni–YSZ anode structure is represented by an elementary reaction mechanism that incorporates steam and dry reforming as well as partial oxidation [25,26]. This mechanism involves 42 reactions among 6 gas-phase species and 12 surface-adsorbed species. However, the mechanism does not specifically incorporate deposit-formation reactions.

Because the porous barrier layer is assumed to be chemically inert, only the gas-phase transport is considered within the barrier (Dusty-gas model). Electrochemical charge transfer is assumed to proceed at the interfaces between the electrodes and the dense electrolyte. The effective active area of the triple-phase region is taken as an empirical parameter, which is incorporated into the exchange current density i^*_O. The model assumes that the charge transfer at the anode–electrolyte interface proceeds only through H_2, which is produced as a result of reforming chemistry within the anode structure [21,27]. Direct charge transfer via CO is neglected, assuming it to be much slower than the H_2 charge transfer. Because the global water-gas shift reaction ($CO + H_2O \rightleftharpoons CO_2 + H_2$) remains nearly equilibrated, some of the CO that is formed via the reforming process is converted to H_2 and CO_2 via water-gas shift processes on the Ni catalyst.

6. Results and discussion

A particular anode-supported tubular cell is used to explore scale-up approaches and alternative operating conditions for an EPOX system. The tube walls nominally have the same dimensions as the MEA in the button-cell experiments. The tube is 25 cm long, has an inner diameter of 0.8 cm, and a wall thickness of approximately 1175 μm. The electrolyte is 10 μm thick YSZ and the cathode is 40 μm thick porous LSM–YSZ. In the initial 7.5 cm of the tube, the tube wall is composed of a 400- μm thick barrier layer and 725 μm of Ni–YSZ. Downstream of the barrier section the anode is 1125 μm thick porous Ni–YSZ (i.e., the 400 μm barrier is replaced with 400 μm Ni–YSZ). The model assumes that air flows through an annular region outside the EPOX tube.

Thermal conductivities of the anode, cathode, and electrolyte are taken to be 11.0, 6.23, and 2.7 W m^{-1} K^{-1}, respectively [28]. The effective thermal conductivity of the MEA structure is estimated to be $\lambda_m = 10.5$ W m^{-1} K^{-1}. Table 1 lists all other parameters that describe the MEA structure.

Nominal operating conditions are based on an inlet fuel mixture of 97% CH_4 and 3% H_2O. Both fuel and air enter the system at 800° C and atmospheric pressure. The effects of the inlet velocity, barrier length, and operating cell potential on the cell performance are investigated. The nominal cell potential is $E_{cell} = 0.7$ V. The nominal fuel inlet velocity is 60 cm s^{-1}. Inlet air velocity is 720 cm s^{-1}, which supplies roughly double the oxygen required to fully oxidize the fuel. The exterior of the EPOX tube assembly (i.e., Fig. 2) is assumed to be insulated, with heat entering and leaving the system only via the gas flows. Because fuel and air enter at 800 °C, an external heat exchanger is needed to preheat the incoming gas streams.

Fig. 5 illustrates major aspects of the model solution for the nominal case. The middle panel shows gas-phase species composition along the length of the tube. The lower panel shows profiles of current density, temperatures of the fuel and air flow, and the MEA temperature as functions of axial position in the tube. The upper panels show gas-phase mole fractions within the anode pore spaces and the adsorbed species coverages on the Ni catalyst surface within the Ni–YSZ anode structure at three axial positions along the tube. The bottom of the upper graphs is at the fuel

channel–anode interface and the top is at the interface between the anode and dense electrolyte.

Consider first the gas flow in the entrance region where the barrier layer is in place. The CH_4 concentration drops as fuel is consumed and products H_2, H_2O, CO, and CO_2 are formed. The CH_4 consumption rate (and product production rate) is relatively low, compared to the section just downstream of the barrier region. This behavior is due to the gas-transport impediment offered by the barrier. The upper panel (at $x = 3$ cm) shows important characteristics of the barrier layer. The distinct change in gradient at the interface between the barrier and the Ni–YSZ is caused by the relatively high gas-phase diffusion resistance offered by the barrier. When CH_4 first encounters Ni, the H_2O levels are relatively high. This is because the barrier impedes the flux of CH_4 toward the dense electrolyte and impedes the flux of steam toward the fuel channel. The major result is that deposit formation is inhibited (hopefully eliminated) in regions where Ni would catalyze coking. In this case, the barrier is designed to insure that in the Ni–YSZ material the gas-phase composition is such that there is no solid carbon (graphite) formed at equilibrium [18].

Within the Ni–YSZ portion of the tube structure, CH_4 is catalytically reformed to produce CO and H_2. The H_2 participates in charge-transfer chemistry, producing H_2O. On the Ni catalyst surface, the H_2O participates in two important catalytic processes. One is to supply the steam needed for CH_4 reforming. The second is to promote water-gas shift chemistry, which reacts CO and H_2O to produce H_2 and CO_2. The CO_2, which is ultimately a reaction product, also participates in the dry reforming of CH_4 to produce CO and H_2. It is evident from the gas-phase profiles within the barrier and Ni–YSZ layers that there is a net flux of CH_4 into the porous anode structure and a net flux of all other species back into the fuel flow within the tube. The right-hand sides of the upper panels show

the surface adsorbates on Ni. Within the barrier layer, where there is no Ni, surface adsorbates are not computed. The results predict that the Ni surfaces are approximately 40% open, with the primary adsorbates being CO(Ni) and H(Ni).

Along the length of the barrier section, the current density decreases. This is primarily a result of fuel consumption. The temperatures of the gases and the MEA initially increase and then decrease near the end of the barrier section. This behavior is the result of a competition between decreasing endothermic reforming activity (leading to higher temperatures) and lower current density (leading to lower temperatures).

Fuel is depleted and diluted as it flows through the tube. At some point the steam–carbon ratio becomes sufficiently high that equilibrium does not favor solid-carbon formation. Once this condition is achieved, the barrier layer is no longer needed and can be removed. Immediately downstream of the barrier-layer section, the barrier layer is replaced by an increased thickness of Ni–YSZ support structure. In this region, the porous-media gas-phase diffusion resistance is reduced because of the relatively more open structure of the Ni–YSZ. Also, because the Ni–YSZ structure is thicker, more Ni catalyst area is available. Consequently, the reforming rates are increased. The increased rates of H_2 and CO levels in the fuel channel are evidence of the increased reforming activity.

Consider the upper panel at an axial position of 8 cm, which shows the gas-phase composition profiles within the Ni–YSZ. The CH_4 profile is maximum at the inner tube wall, and minimum at the dense electrolyte. The CH_4 is consumed by reforming within the Ni–YSZ structure. Both the H_2 and CO profiles have peaks within the Ni–YSZ, providing fluxes toward the dense electrolyte and toward the gas flow within the tube. For an EPOX application this is the desired result. That is, some of the H_2 is used to produce electricity and the remainder is delivered to the flow channel to form the
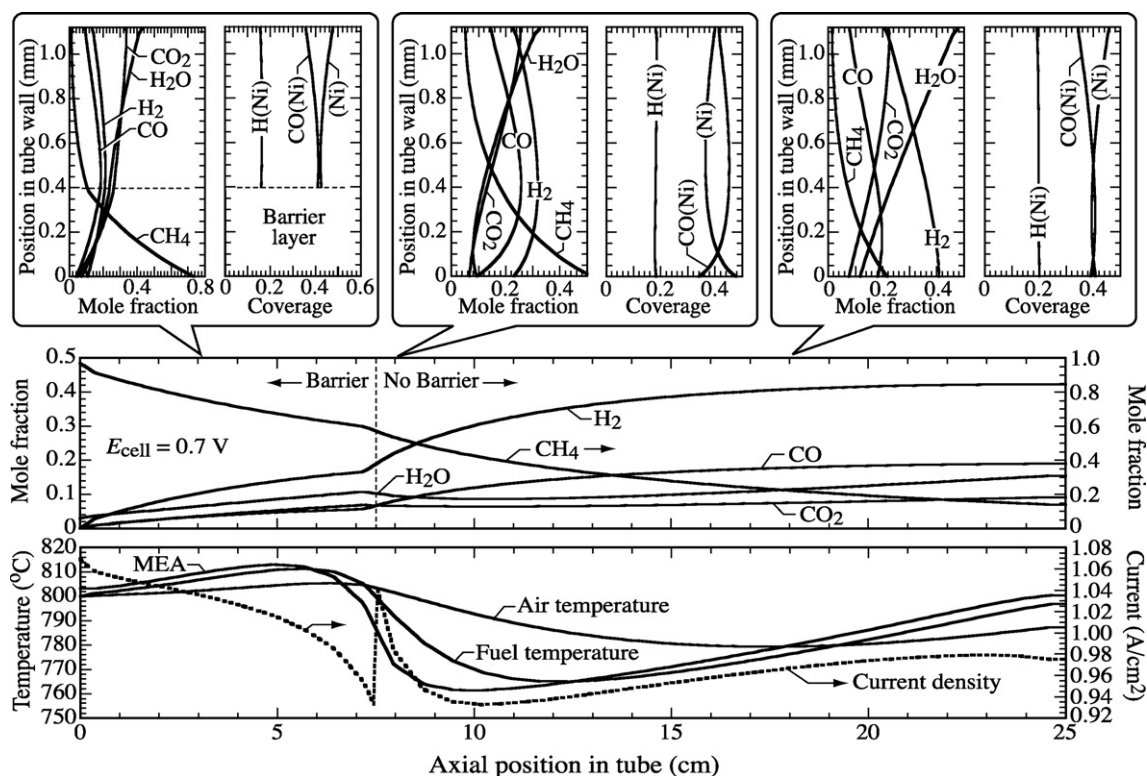
Fig. 5. Solution profiles for the nominal tube geometry and operating conditions. The middle panel shows gas-phase composition of the fuel stream along the channel length. The lower panel shows the local current density, temperatures of the fuel and air streams and the MEA structure as functions of axial position. The upper panels show gas-phase composition in the pore spaces and the adsorbed-species coverages on Ni surfaces within the Ni–YSZ anode at three axial positions along the tube. The bottom of these graphs is at the channel interface and the top is at the dense-electrolyte interface.

desired syngas. The net production of electricity forces the production of CO_2 and H_2O. Some of the CO_2 and H_2O products are also transported into the flow channel. However, with syngas as a desired product, the CO_2 and H_2O yields should be as low as possible.

Immediately downstream of the barrier section, the current density increases sharply. Also, the gas-phase and tube temperatures decrease. Both effects are due to increased reforming activity. The energy needed to support endothermic reforming is supplied from the gas and the walls, which decreases their temperatures. However, the increased reforming produces more H_2, which increases current density via increased charge-transfer rates. The increased current density, in turn, tends to produce heat via ohmic losses and charge-transfer inefficiencies. Early in the non-barrier section, the reforming endotherm dominates and causes lower temperatures. The temperature gradients are highest near the transition between the barrier and non-barrier sections. Although the temperature gradients are modest, they do increase stresses in the materials, which potentially contribute to degradation or damage.

In downstream sections of the tube, the fuel is increasingly depleted and the syngas composition achieves a maximum. However, because the syngas participates as a fuel-cell fuel, extending the tube would cause the syngas to be consumed. The gas and tube temperatures increase in the downstream section of the tube because endothermic reforming activity decreases as fuel is consumed. Moreover, as some syngas is consumed electrochemically, ohmic heating and other polarization losses contribute to increased temperature.

6.1. Effects of the inlet velocity

In addition to other parameters and operating conditions, inlet fuel velocity significantly affects the EPOX performance. The nominal cell geometry and operating conditions are set to maximize syngas output. Either increasing or decreasing inlet fuel velocity decreases the syngas output. Increasing velocity reduces residence time, leading to less reforming. Decreasing velocity increases residence time, allowing a portion of the already-formed syngas to be consumed by the fuel cell to produce electricity.

Fig. 6 shows predicted gas-phase profiles for two situations, comparing them to the nominal case. In all cases the cell is operating at $E_{cell} = 0.7$ V. The low-velocity case reduces the fuel inlet velocity from 60 cm s^{-1} to 35 cm s^{-1} and the air velocity from 720 cm s^{-1} to 420 cm s^{-1}. Fig. 7 shows that the low-velocity case leads to a maximum H_2 concentration at about 15 cm into the tube. Assuming that maximum syngas is desired, the tube should be shortened as inlet velocity decreases.

Fig. 7 shows current–density profiles for the nominal and low-velocity cases. Similar to the composition profiles, the current density is maximum at around 15 cm. Following this peak, the current decreases as the syngas is consumed and higher levels of CO_2 and H_2O dilute the fuel. Again, with the lower velocity, the tube should be shortened accordingly. Overall system optimization depends upon competing factors. A smaller cell likely reduces capital cost. However, a smaller system also produces less power and syngas. The low-velocity, short-tube, approach has a sharper change in power output near the end of the barrier section, which could deleteriously increase materials stresses.

The inlet velocity also affects cell temperatures. As shown in Fig. 8 the nominal case results in generally lower temperatures and temperature gradients. In the low-velocity case, the temperatures are higher, especially in the downstream regions (beyond 15 cm) where the tube is behaving purely as an SOFC consuming the syngas. Of course, as note above, if low velocity is used then the tube should likely be shortened to about 15 cm. In this case, the
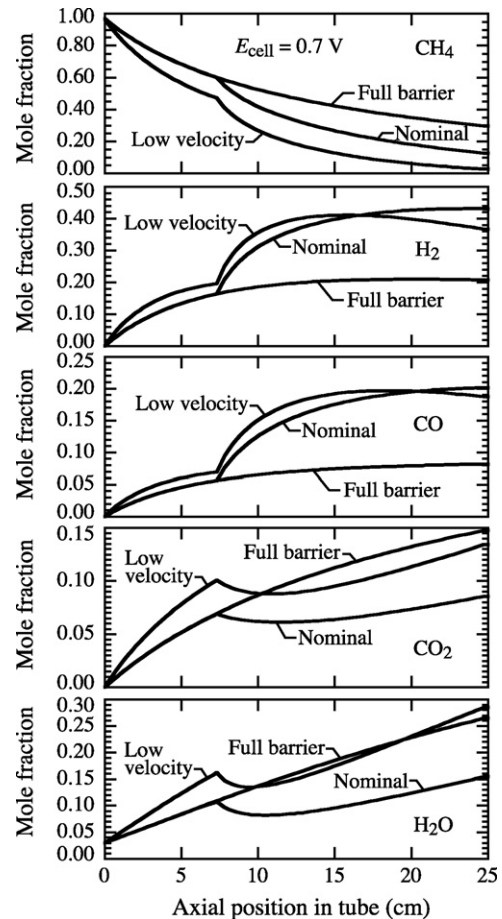
Fig. 6. Axial species profiles for the nominal case and two alternatives. In one case the barrier layer is retained throughout the entire tube length. In this case, the inlet flow conditions are the same as the nominal case. The other case uses the nominal barrier design, but reduces the inlet velocity relative to the nominal case. In all cases, the operating cell potential is uniform at $E_{cell} = 0.7$ V.

low velocity leads to even smaller temperature variations than the nominal case.

6.2. Effects of the barrier layer length

The purpose of the barrier layer is primarily to capture electrochemically produced steam within the porous anode such that the steam–carbon ratio is sufficiently high to prevent carbon deposition on the Ni-based anode. As the steam and CO_2 are transported into the fuel channel, the steam–carbon ratio increases along the channel length and thus relaxes the need for the barrier. From the viewpoint of simplifying fabrication and manufacturing, it would
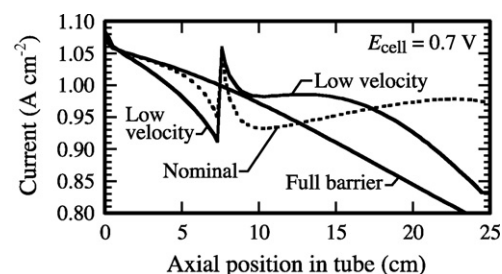
Fig. 7. Axial current–density profiles for the nominal case and the two alternatives noted in Fig. 6.

be preferable to retain the barrier layer for the entire length of the cell. However, as discussed below, the full barrier reduces overall EPOX performance.

The tight pore structure of the barrier layer causes higher transport resistance, which for comparable fluxes to support charge-transfer chemistry, requires larger gas-phase species concentration gradients between the fuel channel and the dense electrolyte. Figs. 6–8 compare solutions for a cell with the barrier extending the entire length of the tube. Otherwise the operating conditions are the same as for the nominal case.

Because the cell structure is uniform throughout tube length, all the solution profiles are smooth. That is, unlike the nominal case, there are no abrupt changes at the interface between the barrier section and the downstream section without a barrier. However, it is also clear from Fig. 6 that the syngas production is considerably diminished. Moreover, as illustrated in Fig. 7 the full-barrier design causes far greater variation in current density than in the nominal case. Finally, Fig. 8 shows that the temperature variations are substantially greater when a full barrier is used. Overall, from the viewpoint of EPOX performance, it is clear that the barrier layer should be used only where it is needed to prevent deposit formation.

6.3. Effects of cell potential

As shown in Fig 1, increasing the O^{2-}/CH_4 flux ratio increases fuel oxidation toward H_2O and CO_2. As the operating potential decreases (i.e., increasing O^{2-} flux), then increased fuel and air flow rates are needed to maintain the molar-flux ratios needed to maximize syngas production (i.e., $O^{2-}/CH_4 \approx 1.2$). For example, at an operating potential of $E_{cell} = 0.5$ V, the nominal cell requires fuel and air inlet velocities of 100 cm s^{-1} and 1200 cm s^{-1}, respectively. At an operating potential of $E_{cell} = 0.6$ V, the nominal cell requires fuel and air inlet velocities of 85 cm s^{-1} and 1020 cm s^{-1}, respectively.

Fig. 9 shows the predicted species profiles for the nominal cell operating at different cell potentials. As noted in the previous paragraph, the velocities are varied to maintain near-optimal molar-flux

Fig. 9. Species profiles for the nominal tube and operating conditions, but at the operating cell potentials (E_{cell}) of 0.5 V, 0.6 V, and 0.7 V.

ratios. As a result, and assuming appropriate velocities, the effect of cell potential upon syngas production is relatively weak.

Fig. 10 compares the current and power densities for the cell operating at 0.5 V, 0.6 V, and 0.7 V. In each case, the fuel and air velocities are adjusted to maintain near-optimal molar-flux ratios (i.e., maximizing syngas yield). As the cell potential decreases, the net current density increases. Moreover, lower cell potentials cause significantly more axial variation in the current–density profiles.

Fig. 10. Current and power densities for the nominal cell operating at cell potentials (E_{cell}) of 0.5 V, 0.6 V, and 0.7 V. For each operating potential, the fuel and air inlet velocities are adjusted to maintain the molar-flux ratio near the optimal value of 1.2.
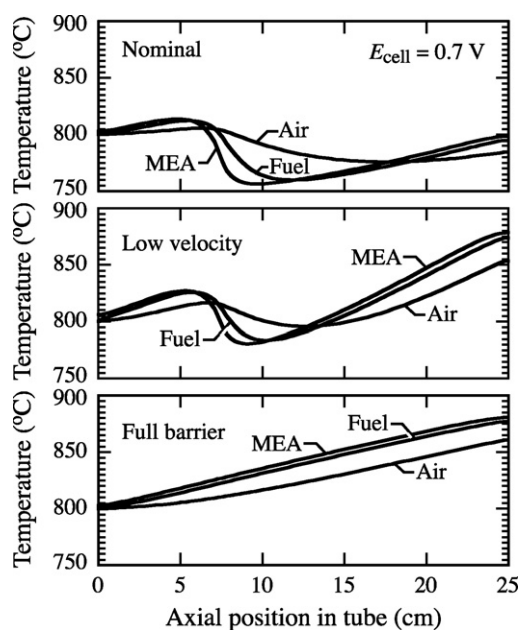

Fig. 8. Temperature profiles for the MEA solid phase, fuel stream, and air stream. Results are shown for the nominal case and the two alternatives noted in Fig. 6.
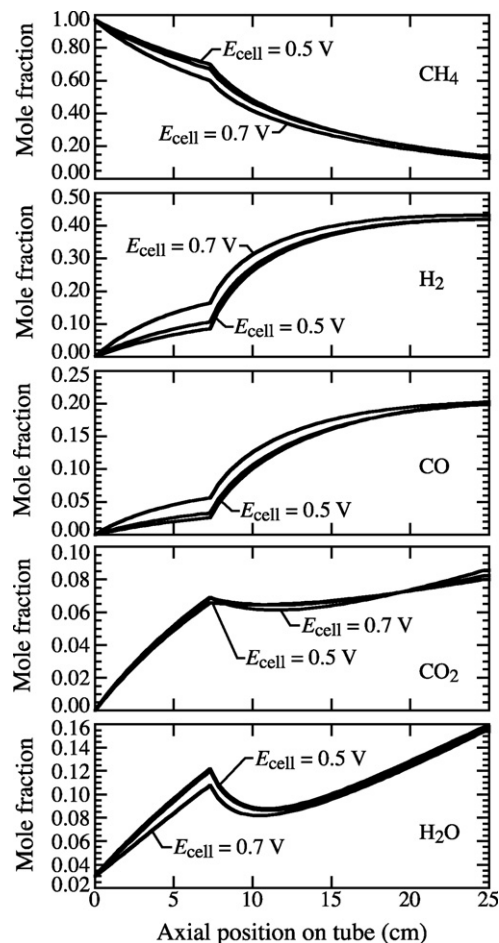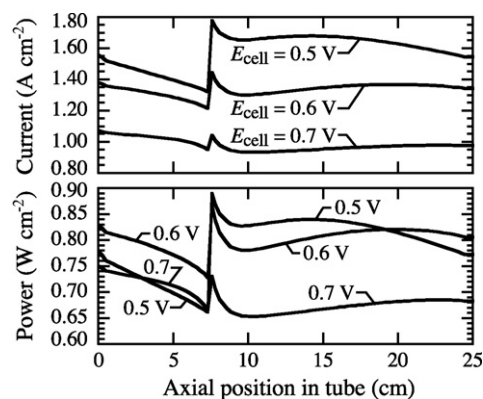
Fig. 11. Temperature profiles for the nominal cell operating at cell potentials (E_{cell}) of 0.5 V, 0.6 V, and 0.7 V. For each operating potential, the fuel and air inlet velocities are adjusted to maintain the molar-flux ratio near the optimal value of 1.2.
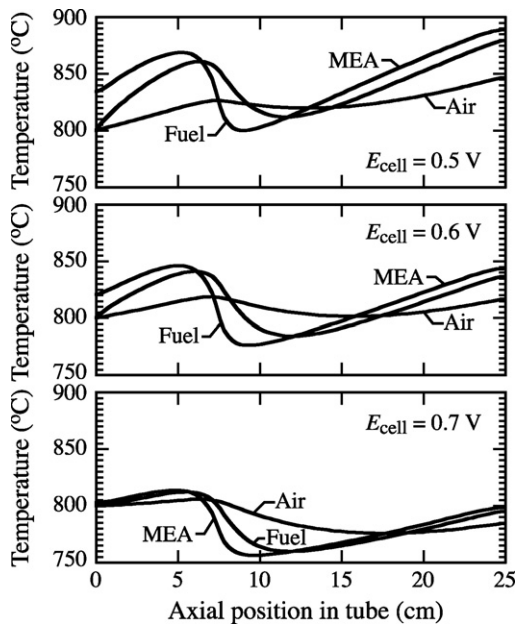
Assuming spatially uniform cell potential, the power densities follow directly from the current densities. The lower panel of Fig. 10 shows considerable variation in power density as the operating potential varies.

Higher current densities contribute to greater ohmic heating and other polarization losses, leading to increased temperatures. Fig. 11 compares the temperature profiles for three operating potentials. Although the general shapes of the temperature profiles are similar, the absolute temperatures are quite different. As the operating potential decreases, the fluid and cell temperatures increase considerably. Moreover, lower cell potential lead to much greater temperature variations along the length of the cell. Endothermic reforming chemistry moderates the temperature increases. Nevertheless, the increased heating associated with internal losses at high current density more than offset the heat needed to support reforming.

The lower panel of Fig. 11 shows that for the nominal case, the fuel and air enter and leave the system at approximately 800 °C. This means that the system is approximately thermally balanced. In other words, the heat generated via ohmic and other polarization losses are roughly just sufficient to deliver the heat needed to support endothermic reforming. However, at the system level, additional heat would be needed to preheat the inlet gases. Some, but clearly not all, of the needed heat can be recovered from the exhaust.

7. Conclusions

A computational model is developed and applied to investigate the characteristics of an EPOX system that is intended to produce both electricity and syngas. Generally speaking, the EPOX device considered herein is an SOFC that is operated somewhat differently from an ordinary SOFC. The current EPOX device is a tubular SOFC in which methane is internally reformed within the anode structure. Fuel flow rates are sufficiently high that all the syngas formed

cannot be electrochemically oxidized. The systems can be designed and operated such that the exhaust stream is dominantly a mixture of H_2 and CO (i.e., syngas), but also containing some H_2O, CO_2, and possibly some unreacted hydrocarbons.

The approach in the present paper begins with experimental EPOX results obtained in a small button-cell configuration. A model for the planar button cell is used to establish physical and chemical parameters that characterize the MEA performance. These same parameters are then used in another model that represents a larger tube-based EPOX device that uses the same MEA architecture. Deleterious carbon-deposit formation is an important consideration when exposing hydrocarbons to high-temperature Ni surfaces. A barrier-layer design is used to inhibit carbon deposits.

The results show that a scaled-up tube-based EPOX system is certainly feasible. There are numerous design and operating alternatives that can be used to optimize performance. Physically based models, together with laboratory-based validation, provide a valuable tool that can assist the design and development process.

References

[1] F. Alcaide, P. Cabot, E. Brillas, J. Power Sources 153 (2006) 47–60.
[2] G. Marnellos, M. Stoukides, Solid State Ionics 175 (2004) 597–603.
[3] K. Sundmacher, L.K. Rihko-Struckmann, V. Galvita, Catal. Today 104 (2005) 185–199.
[4] C. Athanassiou, G. Pekridis, N. Kaklidis, K. Kalimeri, S. Vartzoka, G. Marnellos, Int. J. Hydrogen Energy 32 (2007) 38–54.
[5] T. Ishihara, T. Yamada, T. Akbay, Y. Takita, Chem. Eng. Sci. 54 (1999) 1535–1540.
[6] V.A. Sobyanin, V.D. Belyaev, V.V. Galvita, Catal. Today 42 (1998) 337–340.
[7] G.L. Semin, V.D. Belyaev, A.K. Demin, V.A. Sobyanin, Appl. Catal. A: Gen. 181 (1999) 131–137.
[8] V.A. Sobyanin, V.D. Belyaev, Solid State Ionics 136–137 (2000) 747–752.
[9] Z. Zhan, Y. Lin, M. Pillai, I. Kim, S.A. Barnett, J. Power Sources 161 (2006) 460–465.
[10] H.E. Vollmar, C.U. Maier, C. Nolscher, T. Merklein, M. Poppinger, J. Power Sources 86 (2000) 90–97.
[11] X. Zhang, S. Ohara, H. Chen, T. Fukui, Fuel 81 (2002) 989–996.
[12] M.R. Pillai, D.M. Bierschenk, S.A. Barnett, Catal. Lett. 121 (2008) 19–23.
[13] F. Starr, E. Tzimas, S. Peteves, Int. J. Hydrogen Energy 32 (2007) 1477–1485.
[14] S. Consonni, F. Viganò, Int. J. Hydrogen Energy 30 (2005) 701–718.
[15] P. Chiesa, S. Consonni, T. Kreutz, R. Williams, Int. J. Hydrogen Energy 30 (2005) 747–767.
[16] E.M. Leal, J. Brouwer, J. Fuel Cell Sci. Technol. 3 (2006) 137–143.
[17] Y. Lin, Z. Zhan, S.A. Barnett, J. Power Sources 158 (2006) 1313–1316.
[18] H. Zhu, A.M. Colclasure, R.J. Kee, Y. Lin, S.A. Barnett, J. Power Sources 161 (2006) 413–419.
[19] H. Zhu, R.J. Kee, J. Power Sources 169 (2007) 315–326.
[20] F. Tietz, Q. Fu, V.A.C. Haanappel, A. Mai, N.H. Menzler, S. Uhlenbruck, Int. J. Appl. Ceram. Technol. 4 (2007) 436–445.
[21] H. Zhu, R.J. Kee, V.M. Janardhanan, O. Deutschmann, D.G. Goodwin, J. Electrochem. Soc. 152 (2005) A2427–A2440.
[22] R.J. Kee, M.E. Coltrin, P. Glarborg, Chemically Reacting Flow: Theory and Practice, John Wiley, 2003.
[23] G.K. Gupta, E.S. Hecht, H. Zhu, A.M. Dean, R.J. Kee, J. Power Sources 156 (2006) 434–447.
[24] E.A. Mason, A.P. Malinauskas, Gas Transport in Porous Media: The Dusty-Gas Model, American Elsevier, New York, 1983.
[25] E.S. Hecht, G.K. Gupta, H. Zhu, A.M. Dean, R.J. Kee, L. Maier, O. Deutschmann, Appl. Catal. A 295 (2005) 40–51.
[26] V.M. Janardhanan, O. Deutschmann, J. Power Sources 162 (2006) 1192–1202.
[27] R.J. Kee, H. Zhu, D.G. Goodwin, Proc. Combust. Inst. 30 (2004) 2379–2404.
[28] T. Nishino, H. Iwai, K. Suzuki, J. Fuel Cell Sci. Technol. 3 (2006) 33–44.